Journal of Materials Chemistry B

ROYAL SOCIETY OF CHEMISTRY

PAPER

View Article Online
View Journal

Check for updates

Cite this: DOI: 10.1039/d6tb00247a

Matrix-bound Tenascin-C directs neuronal differentiation through stiffness-tuned MeHA hydrogels mimicking the spinal cord microenvironment

Rounak Pokharel,[a] Vasanti Dhakate,[a] Jessica Onyak,[a] Elif Ertugral,[b] Chandrasekhar R. Kothapalli [b] and Nic D. Leipzig *[a]

Spinal cord injury (SCI) leads to a complex remodeling of the extracellular matrix (ECM), where Tenascin-C (TNC) is strongly upregulated during the early phases of the injury cascade. While TNC is known to influence neural cell behavior, its functional role and mode of presentation in guiding neuronal differentiation remains unclear. In this study, we developed a stiffness-controlled methacrylated hyaluronic acid (MeHA) hydrogel platform that mimics the mechanical properties of the spinal cord and enables defined matrix immobilization of TNC. *In vivo* analyses showed elevated TNC expression from day 1, with the strongest perilesional signal during the subacute period (1 week–1 month). Using this temporal insight, we investigated the role of matrix-bound *versus* soluble TNC in directing neuronal differentiation of induced spinal cord progenitor cells *in vitro*. Immobilized TNC presented with naïve spinal cord stiffness matched MeHA substrates significantly enhanced neuronal and motor neuron differentiation, as evidenced by increased βIII-tubulin and ISL1 expression, compared to soluble TNC or unmodified controls. These effects were strongly dependent on both ligand concentration and matrix stiffness, highlighting a narrow bioactive window for TNC-mediated signaling (effective window: 100-200 nM; reduced responses at ≥300 nM). Furthermore, bulk 3D MeHA hydrogels functionalized with TNC supported cell viability and sustained neuronal differentiation, demonstrating translational relevance for future scaffold-based neural repair. These findings identify TNC as a matrix-bound bioactive cue that interacts with the mechanical environment to regulate neuronal lineage commitment, providing a framework for designing next-generation biomaterials for neural repair.

Received 30th January 2026,
Accepted 29th April 2026

DOI: 10.1039/d6tb00247a

rsc.li/materials-b

1. Introduction

Spinal cord injury (SCI) initiates a complex series of molecular and cellular events that disrupt the native architecture of the nervous tissue and limit its capacity to regenerate. The primary mechanical trauma is quickly followed by a cascade of secondary processes such as inflammation, oxidative stress, and reactive gliosis, which together amplify the initial damage and promote further neuronal and axonal loss.[1–3] As the tissue stabilizes, the extracellular matrix (ECM) undergoes extensive remodeling to restore mechanical integrity. Although this process is essential for structural containment, it results in the deposition of glycoproteins and proteoglycans that create a dense fibrotic scar.[4,5] The resulting microenvironment becomes biochemically inhibitory and mechanically rigid, forming a barrier that restricts cellular migration and axonal regrowth. Accumulating evidence indicates that both ECM composition and stiffness play a key role in regulating neural cell behavior, differentiation, and lineage specification.[6,7] Understanding how these mechanical and biochemical cues interact is important for the design of biomaterials that can mimic the evolving microenvironment of the injured spinal cord.[8]

TNC represents one of the ECM components that change markedly following injury. It is a large, six armed, multifunctional glycoprotein composed of fibronectin type III and EGF-like domains that allow interactions with integrins, growth factors, and other matrix proteins.[9–13] TNC monomer size is isoform and glycosylation-dependent, with commonly reported molecular weights in the 180–250 kDa range, and these monomers assemble into a hexameric (hexabrachion) complex.[9–13] During development, TNC is abundant in regions of active

[a] Department of Chemical, Biomolecular, and Corrosion Engineering, The University of Akron, Akron, OH 44325, USA. E-mail: nl21@uakron.edu
[b] Department of Biomedical Engineering, Cleveland State University, Cleveland, OH, USA

morphogenesis where it supports cell migration, axon guidance, and tissue organization.[14–17] In the adult central nervous system (CNS), its expression is normally low but rises sharply after trauma or inflammation, including in neuroinflammatory and demyelinating lesions of the human brain and cord,[18] suggesting that it participates in tissue remodeling and repair.[19–21]

Following SCI, TNC expression has been shown to increase near the lesion core during the subacute phase and decreases as the scar matures into the chronic phase.[16,17,22–24] The protein is predominantly expressed by reactive astrocytes and glial cells that line the lesion boundary.[3,25] TNC upregulation is thought to stabilize the wound and modulate inflammatory signaling in the early phase, but prolonged expression is associated with the formation of a non-permissive matrix that hinders axonal extension and regeneration permanently.[12,16] These contrasting effects imply that the biological activity of TNC depends on the biological context and on how it is organized within the surrounding ECM.

Although TNC has been studied in the context of injury and repair, little is known about its mode of presentation, specifically immobilized *vs.* soluble forms, and how the mechanical properties of the matrix might influence its activity. *In vivo*, TNC is present in both soluble and matrix-associated forms, yet the way these modes of presentation affect neural lineage commitment has not been thoroughly investigated.[6,7] Furthermore, the mechanical signature of the spinal cord changes dramatically after injury, shifting from the compliant tissue of the healthy cord to the stiffer scar that develops during chronic stages (6 month) with Young's Elastic Modulus (E_Y) reported values spanning the low-Pa to sub-kPa range depending on injury stage, region, and model.[26–29] How cells perceive and respond to TNC under these evolving conditions remains poorly understood.

To explore this relationship, we first examined the temporal and spatial pattern of TNC expression following SCI. A thoracic contusion SCI model was selected because it reproduces key pathological features of clinically prevalent traumatic SCI.[30] We then modeled these conditions *in vitro* using a tunable methacrylated hyaluronic acid (MeHA) hydrogel system that replicates spinal-tissue stiffness (approximately 100–500 Pa as measured by AFM, spanning the sub-kPa mechanical range of native and injured spinal cord tissue; Fig. 2A) and allows controlled presentation of TNC. Finally, we extended these studies into bulk three-dimensional constructs to evaluate the relevance of TNC signaling within a physiologically representative environment. We hypothesized that matrix-bound TNC, when presented within a compliant matrix that mimics naïve spinal tissue, would promote neuronal differentiation and provide insight into how ECM-derived cues regulate neural repair.

2. Experimental section

2.1. Spinal cord injury model and tissue processing

All animal procedures have been conducted in compliance with the University of Akron and Institutional Animal Care and Use Committee (IACUC) guidelines. Adult male Fisher 344 rats (10–12 weeks old) were anesthetized with 1–3% isoflurane, which was maintained throughout the procedure. A midline incision was made along the spine, and the muscles were dissected to expose the spinal column. A laminectomy was then performed at the T8 level, followed by a 250-kdyn contusion injury using the Infinite Horizon Impactor (Precision Systems and Instrumentation). After surgery, the wound was closed with absorbable sutures and Michel clips. The rats were terminally anesthetized using peritoneal administration of FatalPlus, followed by transcardial perfusion with phosphate-buffered saline (PBS), spinal cords were collected on 1 day, 1 week, 1 month, and 6 month after injury along with sham (laminectomy only) and naïve controls (n = 3 per group).

For atomic force microscopy (AFM) and RNA analysis, rats were transcardially perfused with only saline. For AFM, fresh 1000 μm sections were collected from the lesion epicenter with a vibratome (VT1000S, Leica, Wetzlar, Germany). Tissues were cryoprotected, embedded in Tissue-Tek optimal cutting temperature (OCT) compound (VWR Cat. No. 25608-930) and stored at −80 °C overnight. The OCT blocks were then cryosectioned using cryostat (Leica CM1860, Leica Biosystem) at −20 °C into 100 μm slices. These 100 μm slices were used for further AFM analysis detailed below.

For RNA analysis, fresh 500 μm sections were collected from the lesion epicenter with a vibratome. These sections were immediately isolated and immersed in RNAlater (Sigma-Aldrich, Cat. No. R0901-100ML) and stored at 4 °C overnight to stabilize RNA. These samples were then stored at −80 °C for long term storage. These sections were used for gene expression analysis as outlined below.

For immunohistochemistry (IHC) of spinal cord tissues, the OCT blocks were sectioned using cryostat at −20 °C into 20 μm slices and stored at −80 °C until further use. These sections were fixed with 4% PFA, permeabilized with 0.1% Triton X-100, and blocked with 1% FBS, then incubated overnight at 4 °C with mouse monoclonal anti-Tenascin-C (Santa Cruz Biotechnology, Cat. No. SC-25328; 1 : 200 dilution). Next Alexa Fluor 488 Goat Anti-Mouse IgG (Invitrogen, Cat. No. A11001; 1 : 500 dilution) was used as the secondary antibody. Nuclei staining was performed using 10 μM Hoechst (Invitrogen) for 7 min, rinsed, and mounted using Prolong Gold (Thermo Fisher Scientific), images were taken with a confocal system (A1 plus, Nikon, Minato, Tokyo, Japan), with gain and laser power settings kept constant among samples.

2.2. Atomic force microscopy

Mechanical properties of freshly sectioned rat spinal cord were analyzed using a high-performance MFP-3D-Bio atomic force microscope (AFM; Oxford Instruments, Santa Barbara, CA, USA). Tip-less AFM cantilevers (ARROW-TL1Au, Nanoworld, nominal spring constant: 0.03 N m^{-1}) were modified by gluing a 25-μm polystyrene bead as we described earlier.[31] Force–distance curves were conducted with a constant scan rate of 0.3 Hz at a setpoint of 1 nN within the injury T8 site – on one month post-injury tissue sections. One month sham tissue sections were subjected to the same approach to determine

the stiffness, serving as controls. E_Y was calculated from curves at an indentation depth of approximately 500 nm using the Hertzian model.

2.3. Polyacrylamide and methacrylated hyaluronic acid hydrogel preparation

To control the stiffness of the surface, polyacrylamide (PAA) hydrogels of varying stiffness were prepared as described by Shi and Janmey.[32] Based on our previous work,[33] we prepared two PAA formulations using differing acrylamide and bis-acrylamide concentrations (soft: 6.0% acrylamide/0.058% bis-acrylamide; stiff: 7.5% acrylamide/0.099% bis-acrylamide) to produce hydrogels with E_Y targeted at 100 Pa and 500 Pa, these are referred to as soft and stiff, respectively. These stiffnesses were chosen to replicate the bulk E_Y corresponding to naïve and injured SCI tissues. To confirm desired E_Y, mechanical testing of PAA hydrogels was performed *via* a TA Ares G2 rheometer using a 40 mm parallel-plate setup. Frequency sweep tests (1% strain, 1–100 Hz) were conducted to determine the storage (G'), and complex (G^*) moduli as seen in SI, Fig. S1. E_Y was calculated from G^*, assuming a Poisson ratio of 0.5 using the relation

$$E_Y = 2G^*(1 + \nu)$$

where G^* is the complex shear modulus obtained from rheological measurements, and ν is the Poisson's ratio, assumed to be 0.5 for incompressible hydrogels. Stiffness ranges corresponding to healthy and injured spinal cord tissue were selected for subsequent experiments, representing what are referred to as 'soft' and 'stiff' conditions.

To provide biomimetic surface coating, methacrylated hyaluronic acid (MeHA) was synthesized following the method of Burdick *et al.*[34] Briefly, 1% (w/v) hyaluronic acid (Biosynth, 9067-32-7) was dissolved in deionized water, and methacrylic anhydride (~20-fold molar excess) was added while maintaining pH 8.0 with 1 M NaOH. The reaction was stirred for 24 h at 4 °C. The product was purified by dialysis against deionized water for 2–3 days and lyophilized to obtain dry MeHA. The degree of methacrylation (DoM) was determined to be 11% by ^{1}H NMR spectroscopy. The DoM was calculated from the ratio of the integrated vinyl proton peaks of the methacrylate group (δ 5.60 and 6.10 ppm, 2H total per methacrylate substituent) to the integrated *N*-acetyl methyl proton peak of the hyaluronic acid *N*-acetylglucosamine (GlcNAc) backbone repeat unit (δ ~ 2.0 ppm, 3H per repeat unit). (SI, Fig. S2).

For coating, 1% (w/v) MeHA and 0.1% (w/v) lithium phenyl-2,4,6-trimethylbenzoylphosphinate (LAP; Sigma-Aldrich, Cat. No. 900889) were dissolved in deionized water. A thin layer of the solution was evenly distributed over preformed PAA hydrogels and placed on a shaker for uniform coverage. The constructs were cross-linked under UV light (405 nm, 25 mW cm^{-2}) for 3 min, and hydrogel discs were punched and sterilized. The morphology of the cross-linked hydrogels was examined by scanning electron microscopy after lyophilization and gold sputter coating.

2.4. Tenascin-C production and modification

TNC was produced from U251MG human glioblastoma cells (Sigma, Cat. No. 09063001-1VL) following a protocol adapted from Aukhil *et al.*[35] Briefly, U251MG cells were cultured in DMEM high glucose (Thermo Fisher, Cat. No. 12660012) supplemented with 5% fetal bovine serum (FBS; Sigma, Cat. No. F2442-100ML) and 1% penicillin–streptomycin (Sigma, Cat. No. P4458-100ML) at 37 °C and 5% CO_2. Once flasks reached confluence, conditioned medium was collected every 3 to 4 days for up to 14 days from eight to ten T-75 flasks and stored at 4 °C with protease inhibitor (Thermo Scientific, A32955) until processing.

Conditioned medium was cleared *via* centrifugation at 70 000 × *g* for 30 min at 4 °C. The supernatant was titrated with 37% ammonium sulfate (Thermo Scientific, J64419.A3) to saturation (22.1 g per 100 mL medium) and gently stirred at room temperature for 30 min to precipitate proteins. The suspension was next centrifuged again at 70 000 × *g* for 30 min, and the resulting pellet was resuspended in sterile 0.2 M ammonium bicarbonate (Sigma-Aldrich, 09830), pH 8.2 (1 mL per 100 mL original medium). After a third centrifugation step at 70 000 × *g* for 30 min, the supernatant was loaded onto a Sephacryl S-500HR size exclusion column (Cytiva, Cat. No. 17-0613-10) equilibrated with 0.15 M NaCl, 0.02 M Tris, pH 7.9, and 0.02% sodium azide. Fractions were automatically collected using an ÄKTA purifier P-900 system (GE healthcare, now Cytiva) *via* UV absorbance monitored at 280 nm shown in SI, Fig. S3. Protein-containing fractions were pooled and dialyzed overnight at 4 °C against 0.15 M NaCl using Spectra/Por2 dialysis membranes (12–14 kDa MWCO; VWR, Cat. No. 25218-468). The dialyzed solution was concentrated to the desired volume using Amicon centrifugal units (100 kDa MWCO, Millipore, Cat. No. UFC9100), aliquoted, and stored at −80 °C until further use.

TNC content was confirmed and quantified by ELISA (Enzyme-linked Immunosorbent Assay) (Antibodies-Online, Tenascin C ELISA kit, Cat. No. ABIN6959885) according to the manufacturer's instructions, total protein concentration was also measured using a Bradford protein assay (Thermo Fisher, Cat. No. 23200).

To introduce functional groups for immobilization, purified TNC was modified using acrylic acid *N*-hydroxysuccinimide (NHS) ester (Santa Cruz, CAS 38862-24-7). Tenascin-C was diluted into Tris–HCl buffer to a final volume of 5 mL. Acrylic acid NHS ester was dissolved immediately before use and added to the protein solution at a molar excess relative to available lysine residues. The reaction was allowed to proceed overnight at 4 °C on a nutator to maintain gentle mixing. The following day, unreacted NHS ester was quenched by adding Tris–HCl to increase the buffer concentration and incubating for 30 min at 4 °C. The reaction mixture was first dialyzed using Spectra/Por2 dialysis tubing (12–14 kDa MWCO) against 0.15 M NaCl at 4 °C to remove low-molecular-weight byproducts, then concentrated to approximately 4 mL using Amicon centrifugal filters (100 kDa MWCO). The acrylate TNC was aliquoted and stored at −80 °C until use. Conjugation efficiency and protein

recovery were assessed by measuring total protein with the Bradford assay and TNC content using the tenascin-C ELISA kit. These values were used to determine TNC concentration in immobilization solutions SI, Fig. S4 and S5. To assess TNC immobilization efficiency, cumulative release studies were performed on bulk MeHA hydrogels (1% w/v MeHA, 0.1% w/v LAP) prepared under identical UV crosslinking conditions (405 nm, 25 mW cm^{-2}, 3 min) and loaded with either soluble (non-acrylated) or immobilized (acrylated) TNC at equivalent initial concentrations. At each time point (Day 0, 3, 6, 9, and 12), the PBS supernatant ($\sim$1 mL) was fully collected from each hydrogel, replaced with an equal volume of fresh PBS, and returned to incubation at 37 °C. At Day 14, the hydrogel constructs themselves were harvested and digested to quantify retained TNC. TNC concentration in all collected fractions and the final scaffold digest was determined using a sandwich ELISA kit described above. Cumulative release was expressed as a percentage of the initial TNC loading, calculated from the sum of all collected fractions relative to total TNC quantified across all fractions plus the Day 14 scaffold-retained fraction.

2.5. Cell culture and differentiation of human embryonic stem cells

Human embryonic stem cells (H9, WiCell, WA09) (female, age 46, XX karyotype) were maintained under feeder-free conditions in mTeSR1 medium (STEMCELL Technologies) on geltrex-coated plates (Thermo Fisher Scientific, Cat. No. A31804) at 37 °C and 5% CO_2. Differentiation toward posterior motor neuron lineage was carried out according to the protocol of Wind and Tsakiridis (2021), with identical reagents, concentrations, and timing.[36] Briefly, cells were differentiated through four sequential phases using N2B27-based media: Phase 1 (Days 0–3, neuroectodermal induction): FGF2 (20 ng ml^{-1}), CHIR99021 (3 μM), and LDN193189 (100 nM); Phase 2 (Days 3–8, posterior patterning): FGF2 (100 ng ml^{-1}), CHIR99021 (3 μM), LDN193189 (100 nM), SB431542 (10 μM), DMH1 (1 μM), SAG (500 nM), purmorphamine (1 μM), and all-trans retinoic acid (RA; 100 nM); Phase 3 (Days 8–14, ventral spinal cord progenitor specification): SAG (500 nM), purmorphamine (1 μM), RA (100 nM), BDNF (20 ng ml^{-1}), GDNF (20 ng ml^{-1}), and L-ascorbic acid (200 μM); Phase 4 (Days 14–24, motor neuron maturation): same as Phase 3 (BDNF, GDNF, L-acorbic acid) and DAPT (10 μM) supplemented with the γ-secretase inhibitor.

2.6. 2D & 3D culture using MeHA hydrogels

For 2D experiments, VSCP cells were seeded at a density of 8×10^4 cells per cm^2 on MeHA-PAA hydrogels functionalized with TNC, RGD peptide, or unmodified control surfaces at day 10 of differentiation and cultured until day 24 using the media described above. For 3D encapsulation experiments, VSCP cell suspensions (1×10^7 cells per mL) were embedded in 1% w/v MeHA hydrogels containing 0.1% w/v LAP with the same biochemical modifications and crosslinked under UV light (405 nm, 25 mW cm^{-2}, 3 min). Cultures were maintained in posterior ventral spinal cord progenitor induction medium with medium changes every 48 h until day 24. These were then used for further analysis.

2.7. Cell viability and immunocytochemistry

On day 24 of differentiation, cell viability and differentiation were assessed using immunocytochemistry and the PrestoBlue viability assay (Thermo Fisher Scientific, Cat. No. A13261). For cell viability analysis, PrestoBlue Cell Viability Reagent was diluted to 10% (v/v) in N2B27 base medium. For 2D cultures, the reagent solution was added to each hydrogel to fully cover the surface, including blank wells for background subtraction, and incubated at 37 °C for 10 min. Aliquots (100 μL) were transferred to a clear 96-well plate, and fluorescence was measured using an Infinite M200 plate reader (Tecan Life Sciences) at 560 nm excitation and 590 nm emission. For 3D cultures, the diluted PrestoBlue solution was added to cover the hydrogels and incubated at 37 °C for 30 min prior to fluorescence measurement. For all conditions, raw fluorescence values were background-subtracted using blank wells and normalized to the unmodified MeHA control (no ligand), which was set to 100% viability. Values exceeding 100% indicate greater metabolic activity relative to the unmodified control and reflect enhanced cell health or proliferation under the test condition, not a measurement artefact.

For immunocytochemistry, 2D hydrogels were fixed with 4% paraformaldehyde (PFA) for 8 min, while 3D hydrogels were fixed for 30 min to ensure adequate penetration. Samples were permeabilized with 0.1% Triton X-100 for 8 min (2D) or 15 min (3D) and blocked with 1% fetal bovine serum (FBS) for 1 h at room temperature. Samples were incubated overnight at 4 °C with primary antibodies against β-III tubulin, GFAP, FAK, and ISL1. Following washing, samples were incubated with species-appropriate secondary antibodies (1 : 500) for 1 h at room temperature. Samples were washed three times with 1× PBS (15 min per wash), counterstained with 10 μM Hoechst for 7 min, rinsed, and mounted using Prolong Gold (Thermo Fisher Scientific). Detailed antibody information, including host species, suppliers, and dilutions, is provided in Table S1 (SI).

Fluorescence images were acquired using an inverted fluorescence microscope (CKX41, Olympus, Shinjuku, Tokyo, Japan) with identical exposure settings across all conditions. For 3D, images were taken using a confocal system and z-stack for the construct was taken using identical exposer setting in all conditions. Image analysis was performed using ImageJ (NIH) to determine mean signal intensity and cell coverage. For quantification of βIII-tubulin-positive cells (Fig. 2E) and ISL1-positive cells (Fig. 5G), manually a minimum of five randomly selected fields of view per sample (10× objective) was selected and uploaded on Image J software. Total cell counts were obtained from co-registered DAPI-stained images, and the percentage of marker-positive cells was calculated as (positive cells/total DAPI-positive nuclei) × 100. Fluorescence intensity thresholds were defined on control samples and applied consistently across all conditions within each experiment. For neurite morphology analysis, βIII-tubulin immunofluorescence

images were processed using the Fiji distribution of ImageJ. Images were first converted to 8-bit grayscale and binarized using consistent thresholding parameters. The Skeletonize (2D/3D) plugin was then applied to generate skeleton traces overlaying the original fluorescence images. Total neurite length was quantified from the skeleton output using the Analyze Skeleton plugin, and neurite length per cell was calculated by dividing total neurite length by the number of DAPI-positive nuclei in the corresponding field of view. A minimum of five fields per condition were analyzed.

For visualization of βIII-tubulin-positive cells (Fig. 2E) and ISL1-positive cell distributions (Fig. 5G), raincloud plots were generated using R (v4.3) with the ggdist and ggplot2 packages, combining half-violin kernel density estimates with individual data points and mean ± 95% confidence interval summaries.

2.8. Gene expression analysis

For analysis of SCI rat tissue sections, total RNA was extracted using the RNeasy Lipid Tissue Mini Kit (Qiagen, Cat. No. 74804) according to the manufacturer's protocol. The resulting RNA was reverse transcribed with the cDNA synthesis kit (Fisher Scientific, FERK1622). Quantitative PCR was performed on a QuantStudio 3 Real-Time PCR system (Applied Biosystems) using SYBR green detection chemistry (Thermo Scientific, Cat. No. A46110). Primers for TNC (Integrated DNA Technologies) were used and expression levels were normalized to the housekeeping gene GAPDH.

For *in vitro* analysis total RNA was extracted using a RNeasy Mini Kit (Qiagen, Cat. No. 74104) and reverse transcribed with the cDNA synthesis kit. Quantitative PCR was performed using a QuantStudio 3 Real-Time PCR system using SYBR Green detection chemistry. Custom primers for OLIG2, TUBB3, and ISL1 (Thermo Fisher Scientific) were used shown in SI, Table S2, and expression levels were normalized to the housekeeping gene GAPDH.

Relative expression was calculated *via* the ΔΔCt method. For *in vitro* experiments, fold changes were expressed relative to cells cultured on unmodified MeHA control substrates (no added ligand), with GAPDH serving as the endogenous reference gene for normalization. For *in vivo* quantitative PCR (qPCR), fold changes were expressed relative to naïve (uninjured) tissue controls, also normalized to GAPDH.[37]

2.9. Statistical analysis

All experiments were conducted with a minimum of three biological replicates. Each biological replicate (n) represents an independent differentiation experiment, with three technical replicates (S) per condition within each experiment. Data are presented as mean ± standard deviation. Statistical significance between two groups was determined using an unpaired two-tailed t-test. Comparisons between multiple groups were performed using either one-way or two-way analysis of variance (ANOVA) followed by Tukey's *post hoc* test. A p-value < 0.05 was considered statistically significant. Statistical analyses were performed using GraphPad Prism version 10.4.1.

3. Results and discussion

3.1. Temporal regulation of TNC following SCI

To characterize how TNC expression changed over time after SCI, we combined quantitative and histological analyses of a rat contusion model (Fig. 1A–C). Fig. 1A outlines the experimental workflow and impact parameters used to generate a consistent 250-kdyn lesion at T8. Fig. 1B shows TNC mRNA expression across injury timepoints obtained by quantitative PCR and shown as relative fold change, revealing a rise at 1 day post-injury, a pronounced peak at 1 week, sustained elevation at 1 month (no statistically significant difference between 1 day and 1 month, $p > 0.9999$), and reduction toward baseline by 6 month. Fig. 1C presents representative immunohistochemistry images of TNC (green) and nuclei (DAPI, blue) at low (4×) and high (20×) magnifications, showing strong perilesional staining during the subacute phase (1 week to 1 month) and minimal signal in naïve, sham and chronic (6 month post-injury) tissue.

The transient increase in TNC we observed after contusion SCI (beginning to rise as early as 1 day post-injury, reaching sustained elevation across the 1 week, and gradually declining toward 1 month to 6 month) is consistent with TNC behaving as an injury-responsive matricellular ECM protein that is elevated during the subacute remodeling window. Prior studies in SCI models show that altering TNC levels can meaningfully affect lesion biology and axonal growth responses, supporting the idea that TNC is not just a passive marker but an active regulator of repair-associated signaling.[38] In parallel, work across CNS injury contexts shows that TNC is strongly induced by reactive glia and inflammatory cues and can shift ECM organization and cell–matrix interactions during early scar formation, aligning with our strong perilesional staining at 1 week to 1 month.[39] Finally, broader spinal cord scar literature describes the subacute period as a phase of dynamic ECM deposition and innate immune activity, where glycoproteins like TNC contribute to the evolving biochemical environment that can either support or restrict plasticity depending on context, which matches the time window in which we see the strongest TNC signal.[40]

3.2. Stiffness-tuned MeHA-PAA hybrid platform

To investigate how mechanical cues potentially contribute to neural differentiation in a spinal cord-relevant context, we engineered a stiffness-tunable hydrogel platform designed to recapitulate the elastic properties of both healthy and injured spinal cord tissue. Fig. 2A shows the E_Y of sham tissue and injured tissue in 1 month post-injury spinal cord tissues. The differences in E_Y between sham tissue and 1 month post injured tissue are similar to our prior results in rat spinal cord tissues.[33] Meanwhile, the injured regions at 1 month time point are softer compared to regions away from the injury site (sham), reaffirming our hypothesis and prior reports in this regard that such soft tissue post-injury modulates cellular migration, attachment to matrix, and ECM remodeling efforts. Indeed, AFM-based studies of rodent CNS tissue have demonstrated

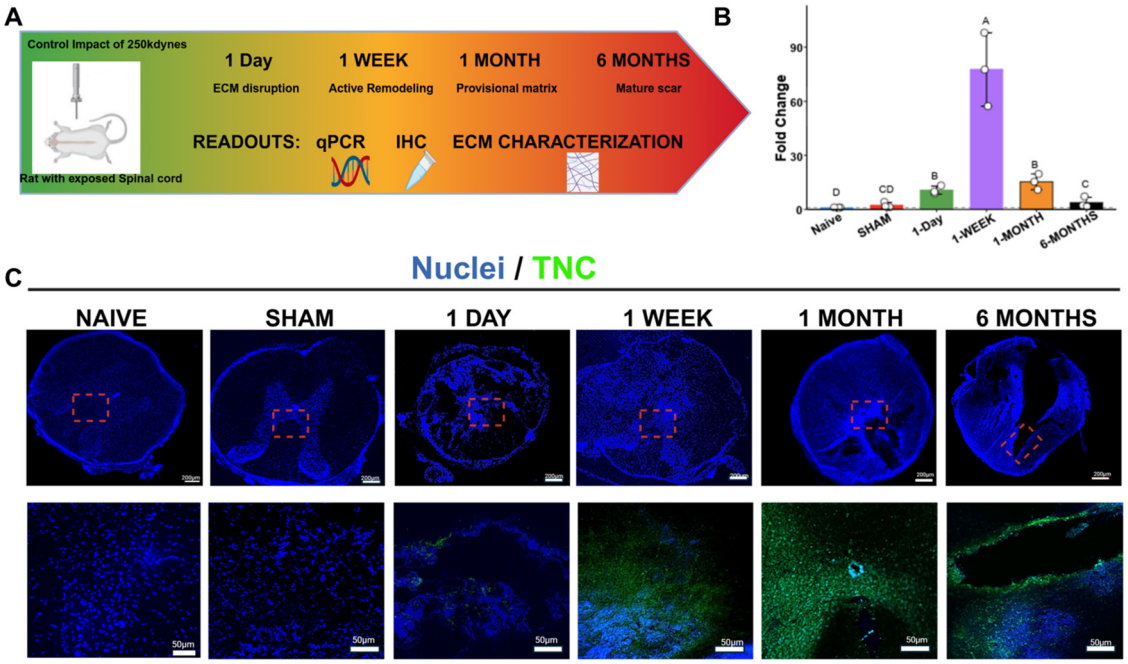

Fig. 1 Temporal regulation of Tenascin-C expression following SCI in rats. (A) Schematic of the T8 contusion SCI model showing a controlled 250-kdyne impact and the experimental timeline. Spinal cord tissue was collected at 1 day (acute), 1 week (subacute), 1 month (intermediate), and 6 month (chronic) post-injury for ECM characterization. (B) qPCR analysis of TNC expression at indicated timepoints, shown as foldchange relative to naïve controls. TNC expression was elevated from 1 day post-injury onward, with sustained high expression through 1 month (no statistically significant difference between 1 day and 1 month) and peak numerical elevation at 1 week, declining toward baseline by 6 month. Data are presented as mean ± SD (n = 3 biological replicates per group). Statistical significance was assessed by one-way ANOVA followed by Tukey's multiple comparisons test. Groups not sharing the same letter are significantly different ($p < 0.05$). (C) Representative immunohistochemistry images of spinal cord cross-sections stained for Tenascin-C (green) and nuclei (blue). Low-magnification images (4×) show overall lesion morphology, with boxed regions indicating areas shown at higher magnification (20×). Robust perilesional TNC deposition was observed during the subacute and intermediate phases (1 week and 1 month), with minimal signal in sham and chronic (6 month) tissue. Scale bars: 200 µm (top row), 50 µm (bottom row).

that glial scars are mechanically softer than surrounding uninjured parenchyma, and that this post-injury softening correlates with altered expression of structural and ECM proteins including GFAP, vimentin, laminin, and collagen IV—components that directly regulate cell adhesion and migration.[33,41]

Based on these E_Y results, hybrid hydrogels were fabricated using a polyacrylamide (PAA) base coated with a thin layer of MeHA as shown in Fig. 2B. In this configuration, the underlying PAA matrix determines stiffness, while the MeHA layer provides a consistent, cell-interactive hyaluronan surface. This design allows the mechanical and biochemical cues to be tuned independently. Scanning-electron micrographs showed a continuous and uniform MeHA coating across all samples, with an average thickness of 199.3 µM, ±13.2 µm (mean ± SD, n = 3) indicating stable crosslinking and surface integrity shown in Fig. 2B. Rheological measurements confirmed that the E_Y increased from soft to stiff formulations (Fig. 2C), with the soft condition measuring ∼150 Pa and the stiff condition ∼500 Pa, corresponding to stiffness ranges representative of injured and healthy spinal cord tissue, respectively.[33] Critically, these measurements were performed on fully hydrated, crosslinked MeHA–PAA composite constructs, meaning the reported E_Y values reflect the effective mechanical properties of the complete system that cells interface with, not the PAA substrate in isolation. The MeHA coating, prepared at 1% (w/v) with an 11% degree of methacrylation and brief UV crosslinking, is itself a highly compliant hydrogel whose storage modulus falls within a comparable range to the underlying PAA layers.[34] This situation is mechanically distinct from the canonical scenario studied by Buxboim *et al.*, in which a thin compliant coating on a rigid substrate produces a large stiffness contrast, causing cells to sense the rigid support through only ∼3–5 µm of soft material.[42] In the present system, both the MeHA surface layer and the PAA substrate exist within the same low-Pa range; no high-contrast stiffness interface is present, and the two layers behave as a mechanically integrated composite as directly reflected by the composite rheology (Fig. 2C). The observed differences in neuronal differentiation outcomes between soft and stiff conditions (Fig. 2D) provide direct empirical confirmation that cells sense and respond to the mechanical distinction between composite substrates. We acknowledge that AFM indentation performed directly on hydrated MeHA-coated surfaces would offer more precise surface-level mechanical characterization and is a priority for future studies.

Stiffness had a clear influence on differentiation outcomes, as immunostaining for βIII-tubulin revealed a greater proportion of neurons on stiff substrates compared with soft ones

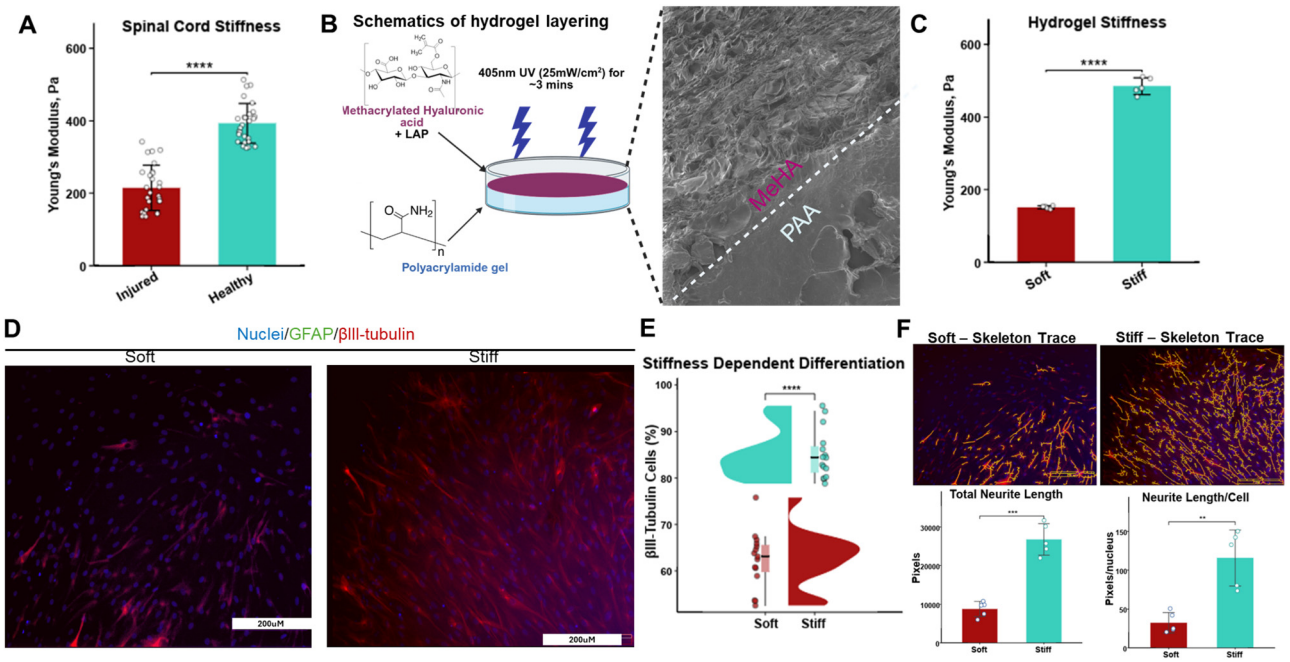

Fig. 2 Stiffness-tuned MeHA–PAA hybrid hydrogel platform recapitulates spinal cord mechanical properties and regulates neuronal differentiation. (A) Young's elastic modulus (E_Y) measurements of native spinal cord tissue and regional stiffness variations at 1 month post-injury. (B) Schematic illustrating the MeHA–PAA hybrid hydrogel system. A stiffness-defining polyacrylamide (PAA) base is overlaid with a thin methacrylated hyaluronic acid (MeHA) layer and crosslinked under UV light (405 nm, 25 mW cm^{-2}, ~3 min), enabling independent control of mechanical and biochemical cues. Representative scanning electron micrograph demonstrates a continuous MeHA coating atop the PAA substrate (dashed line indicates interface). (C) E_Y of soft and stiff hydrogel formulations used for *in vitro* studies (n = 5). (D) Immunofluorescence images of induced spinal progenitors cultured on soft and stiff substrates, stained for nuclei (blue), astrocytic marker GFAP (cyan), and neuronal marker βIII-tubulin (red). (E) Quantification of the percentage of βIII-tubulin-positive cells on soft *versus* stiff substrates, presented as a raincloud plot combining half-violin density distributions with individual data points and mean ± 95% CI. (F) Neurite morphology analysis: representative skeleton trace overlays generated using the Fiji Skeletonize plugin on βIII-tubulin immunofluorescence images (top), with quantification of total neurite length and neurite length per cell (bottom). Data are presented as mean ± SD (n = 3). Statistical significance was assessed by pairwise t-test (** = <0.01, *** = p < 0.001, **** = p < 0.0001).

(Fig. 2D). Cells cultured on the stiff gels displayed longer, more aligned neurites, whereas those on soft gels showed shorter, less organized extensions. GFAP-positive astrocytes were not detected, consistent with a predominantly neuronal phenotype under these differentiation conditions; however, the absence of GFAP staining alone is insufficient to fully exclude other non-neuronal cell types, and additional lineage-specific markers would be required for comprehensive phenotypic characterization. However, quantification of βIII-tubulin-positive cells confirmed a significantly higher proportion of neurons on stiff substrates compared with soft ones (Fig. 2E). To further characterize the morphological differences, neurite outgrowth was analyzed using Fiji's Skeletonize plugin on βIII-tubulin immunofluorescence images, producing skeleton trace overlays that enabled quantification of total neurite length and neurite length per cell (Fig. 2F). Cells on stiff substrates exhibited significantly longer neurites compared with those on soft substrates, consistent with the qualitative observations from immunofluorescence imaging.

The MeHA–PAA hybrid platform allows for decoupling of mechanical stiffness from biochemical surface identity, addressing a key limitation of single-polymer hydrogels where changes in modulus are often accompanied by changes in ligand density or matrix composition.[43,44] This separation is particularly important for modeling spinal cord microenvironments, where tissue stiffness exists within a narrow, low-modulus range and evolves dynamically following injury.[45] The stiffness-dependent enhancement of neuronal differentiation observed here is consistent with prior reports demonstrating that neural progenitor fate and maturation are regulated by substrate mechanics through cytoskeletal tension and mechanotransductive signaling pathways.[46,47] More recent work has further emphasized that mechanical cues act in concert with ECM context to shape lineage specification rather than functioning as isolated instructive signals.[5]

Within this framework, the stiff condition used here likely provides a mechanical context that better supports neuronal maturation compared with more compliant substrates, while maintaining high cell viability. Establishing this stiffness-sensitive baseline was essential for subsequent experiments probing how matrix-bound TNC interacts with spinal-cord–relevant mechanics, as it ensures that observed effects arise from biochemical presentation within a defined mechanical environment rather than from platform-induced stress or instability.[12,44,46] Collectively, these results validate the MeHA-coated PAA system as a robust and tunable 2D platform for investigating how ECM-associated signals cooperate with tissue mechanics to regulate neuronal lineage specification.

3.3. Production and immobilization of bioactive TNC

TNC was purified from conditioned media of U251MG glioblastoma cells using a multi-step protocol combining ammonium sulfate precipitation and size-exclusion chromatography as shown in Fig. 3A, and the protein elution profile shown in Fig. S3 (SI). Quantification by Bradford assay and ELISA confirmed consistent protein recovery across batches, with TNC representing a substantial portion of the total secreted protein (Fig. 3B), Fig. S4 (SI) shows the ELISA standard curve profile used to interpolate the protein concentration. The process yielded protein fraction with minimal contaminants, as verified by SDS-PAGE (Fig. 3C), full SDS-PAGE gel is shown in Fig. S5 (SI).

To enable covalent attachment within MeHA hydrogels, purified TNC was functionalized with acrylic acid *N*-hydroxysuccinimide ester, introducing polymerizable acrylate groups without visible degradation or loss of solubility. The modified protein retained its immunoreactivity in ELISA, indicating that the functionalization preserved epitope integrity (Fig. 3D). Release studies further validated the immobilization efficiency (Fig. 3E). Soluble, non-acrylated TNC exhibited a gradual release of approximately 40% over 14 days, suggesting partial entrapment within the hydrogel matrix. In contrast, acrylated TNC showed minimal release (~10%) over the same period, demonstrating stable covalent incorporation into the MeHA network. This marked difference highlights the effectiveness of the acryloyl-NHS conjugation chemistry in achieving long-term protein retention.

Covalent immobilization of ECM proteins is increasingly recognized as a critical strategy for recapitulating native ECM signaling, particularly in neural tissues where matricellular

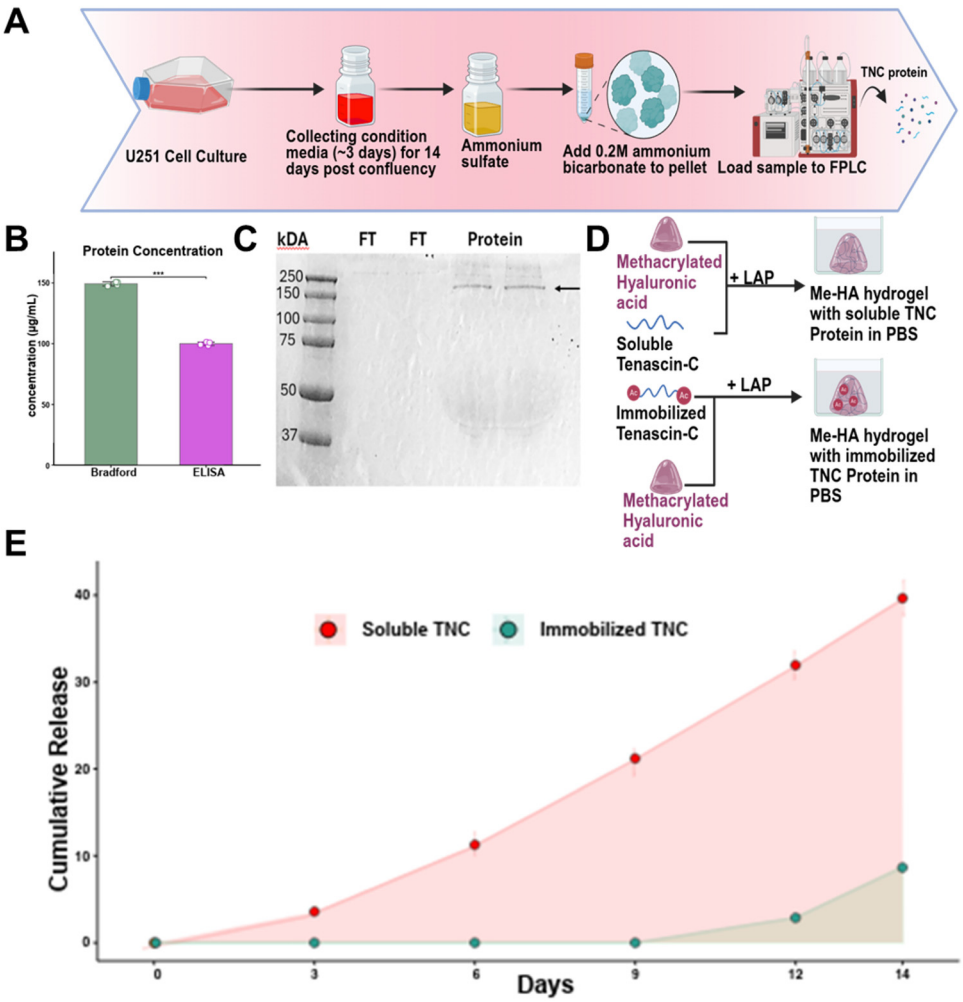

Fig. 3 Production, modification, and immobilization of Tenascin-C within MeHA hydrogels. (A) Schematic overview of Tenascin-C (TNC) purification from conditioned media of U251MG glioblastoma cells using ammonium sulfate precipitation followed by size-exclusion chromatography. (B) Quantification of purified protein by Bradford assay (total protein) and ELISA (TNC-specific), confirming consistent recovery of TNC from conditioned media. Data are presented as mean ± SD (n = 3). Statistical significance was assessed by unpaired two-tailed t-test (*** = $p < 0.001$). (C) Representative SDS–PAGE analysis of purified fractions showing enrichment of TNC with minimal detectable contaminants. (Full SDS-PAGE gel shown in Fig. S5, SI) (D) Schematic illustration of TNC incorporation into methacrylated hyaluronic acid (MeHA) hydrogels *via* covalent crosslinking. (E) Cumulative release profile of soluble and immobilized TNC from MeHA hydrogels over 14 d, showing gradual diffusion-mediated release of soluble TNC and minimal release of immobilized TNC, indicating stable covalent incorporation within the hydrogel network. Data are presented as mean ± SD (n = 4, S = 3).

cues are presented predominantly in a matrix-bound rather than soluble form.[48] TNC is a large, multimeric glycoprotein whose biological activity depends strongly on its mode of presentation, local concentration, and mechanical context.[17,49,50] The purification strategy employed here yielded intact, bioactive TNC, consistent with prior reports using glioma-derived conditioned media as a reliable source of TNC protein.[35]

The marked reduction in release observed for acrylated TNC compared to soluble TNC confirms stable incorporation into the hydrogel network, minimizing diffusion-driven loss over time. This controlled presentation strategy is particularly important for dissecting the role of TNC, as its biological activity is known to depend on local concentration and context within the ECM. By maintaining TNC in a matrix-bound state while decoupling biochemical presentation from bulk material properties, this platform allows the effects of immobilized TNC to be evaluated independently of confounding changes in stiffness or ligand availability. Together, these results establish a robust and tunable system for examining how matrix-bound TNC influences neural differentiation under defined mechanical conditions.

3.4. Matrix-bound immobilized TNC enhances neuronal differentiation in 2D

To determine how biochemical presentation influenced neuronal differentiation, induced spinal cord progenitors were cultured on MeHA–PAA substrates functionalized with either RGD peptides or TNC presented in soluble or immobilized forms across a range of surface concentrations (Fig. 4A).

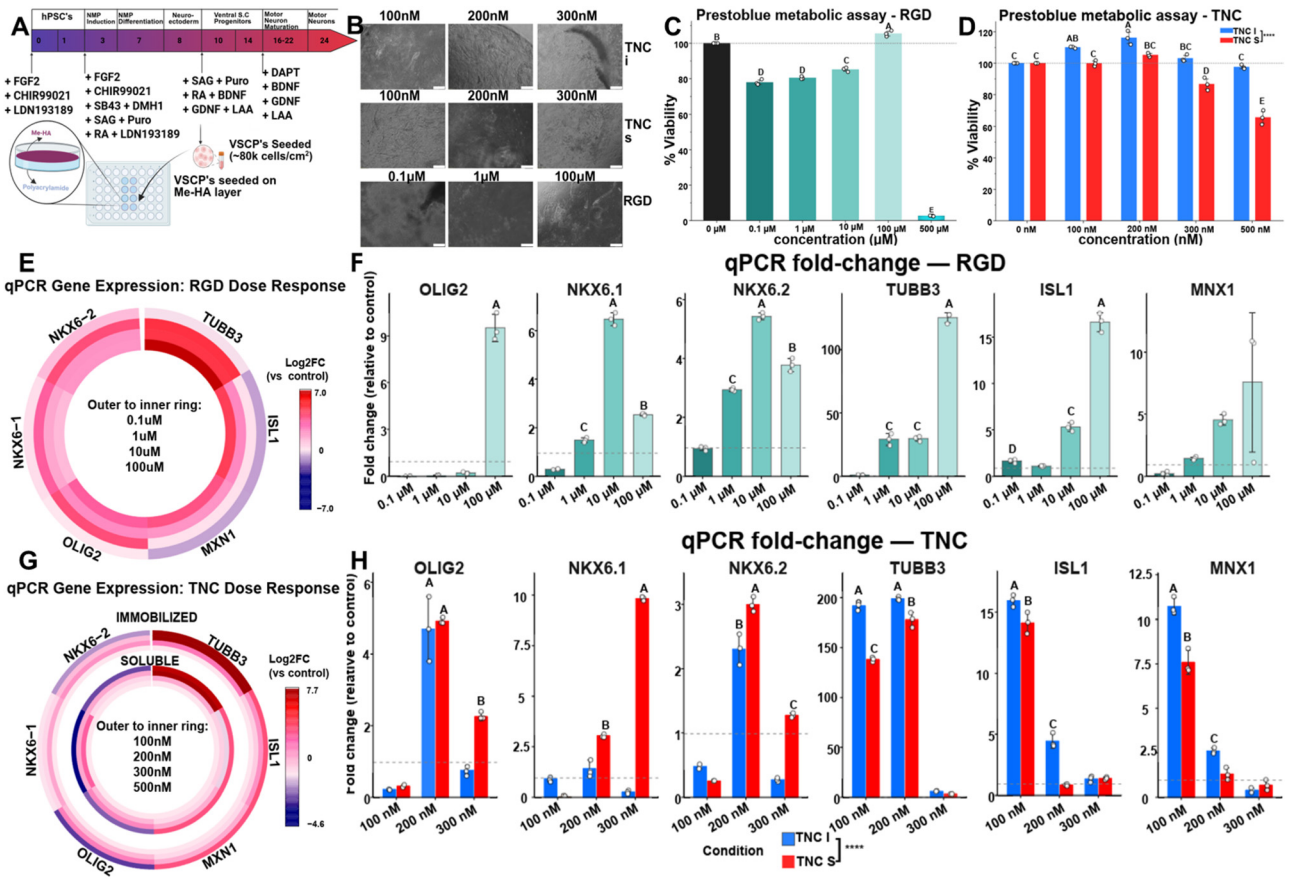

Fig. 4 Matrix-bound Tenascin-C enhances neuronal differentiation in a concentration dependent manner in 2D. (A) Schematic illustrating the differentiation timeline of human pluripotent stem cells into ventral spinal cord progenitors and motor neurons, and their seeding onto MeHA–PAA substrates functionalized with Tenascin-C (TNC) or RGD ligands. (B) Representative brightfield images showing cell adhesion and morphology on substrates functionalized with immobilized TNC (TNC-i), soluble TNC (TNC-s), or RGD across increasing ligand concentrations. Scale bar: 100 μm. (C) PrestoBlue metabolic activity of cells cultured on RGD-functionalized substrates across increasing concentrations. (D) PrestoBlue metabolic activity of cells cultured on TNC-functionalized substrates comparing immobilized (TNC-i) and soluble (TNC-s) presentation across concentrations. (E) Heatmap of qPCR log2 fold-change (*vs.* control) for six neuronal and motor neuron markers (OLIG2, NKX6.1, NKX6.2, TUBB3, ISL1, MNX1) across RGD dose response. (F) qPCR analysis of fold-change expression to no RGD control for individual genes (OLIG2, NKX6.1, NKX6.2, ISL1, TUBB3, MNX1) in cells cultured on RGD-functionalized substrates. (G) Heatmap of qPCR log2 fold-change for the same markers across TNC dose response, comparing immobilized and soluble presentation. (H) qPCR analysis of fold-change expression to no TNC control for the same genes in cells cultured on TNC-functionalized substrates comparing immobilized and soluble presentation across concentrations. All data are presented as mean ± SD (n = 3, S = 3). Groups not sharing the same letter are significantly different ($p < 0.05$) *via* ANOVA with Tukey's multiple comparisons test. Direct comparisons between immobilized and soluble TNC (TNC-i and TNC-s) at the same concentration (**** = $p < 0.0001$).

Brightfield imaging (Fig. 4B) provided qualitative visualization of cell adhesion and morphology across ligand concentrations. Cell density, morphology, and contact area were assessed semi-quantitatively from these images, with PrestoBlue metabolic activity serving as the primary quantitative correlate for concentration-dependent effects. At higher coating densities, cells displayed reduced adhesion and spreading on both RGD and TNC functionalized surfaces, suggesting that excessive ligand density disrupts effective cell–matrix interactions. This type of ligand-density dependence is well established for integrin-binding motifs like RGD, where spacing and availability govern focal adhesion maturation and downstream signaling rather than more ligand means better adhesion.[51] Cell viability assays confirmed this trend as shown in Fig. 4C and D. RGD-modified substrates supported maximal viability at 100 μM, while higher concentrations ($\geq$500 μM) resulted in significant loss of metabolic activity ($p < 0.0001$). In contrast, TNC-functionalized substrates exhibited peak viability at 100–200 nM, with immobilized TNC supporting significantly higher viability than soluble TNC across this range ($p < 0.0001$). Functionalization of both TNC and RGD within the stated surface concentration ranges also led to focal adhesion kinase (FAK) activation, as confirmed by robust FAK staining (Fig. S6A, SI) indicating engagement of integrin-mediated adhesion signaling. RGD is a well-established ligand for several integrins, most prominently αvβ1 and αvβ3, which are known to activate FAK through clustering and focal adhesion maturation.[52,53] In contrast, TNC binds integrins yet promotes transient, migratory adhesion states rather than the stable adhesion characteristic of classical ECM ligands.[1,14,25,54,55] TNC has been shown to bind specific integrin receptors, including α9β1, αvβ3, and α8β1, depending on cellular context and matrix presentation.[49,54,56] Previous studies have shown that matrix-bound TNC can promote integrin-dependent signaling and cytoskeletal remodeling despite its anti-adhesive domains, resulting in downstream activation of FAK and mechanosensitive pathways.[57–61] Together, these findings support that both RGD and immobilized TNC converge on integrin-FAK signaling, while differing in ligand–receptor specificity and downstream effects on neuronal differentiation.

Neuronal differentiation outcomes paralleled the observed viability trends. In RGD-functionalized substrates, increased ligand density promoted neuronal differentiation, with higher concentrations (up to 100 μM) resulting in elevated expression of neuronal marker βIII-tubulin and motor neuron markers ISL1 and MNX1. Similarly, ventral spinal progenitor markers (OLIG2, NKX6-1, NKX6-2) exhibited a concentration-dependent increase, suggesting a largely monotonic relationship between RGD density and lineage specification (Fig. 4E and F). However, excessive RGD ($\geq$500 μM) impaired cell attachment and viability, limiting its functional range.

In contrast, immobilized TNC exhibited a non-linear, dose-dependent effect. At intermediate concentrations (100–200 nM), immobilized TNC significantly enhanced neuronal differentiation, as evidenced by increased βIII-tubulin expression and upregulation of motor neuron markers ISL1 and MNX1 compared to soluble TNC and control substrates (Fig. 4G and H). Notably, peak motor neuron marker expression was observed at 100 nM, while higher concentrations (200–300 nM) preferentially increased ventral progenitor markers (OLIG2, NKX6-1, NKX6-2), indicating a shift toward progenitor maintenance rather than terminal differentiation. At concentrations $\geq$300 nM, neuronal marker expression declined, further supporting the presence of an optimal signaling window for matrix-bound TNC. At 500 nM the RNA yield was low and couldn't be used for qPCR analysis which might suggest a ligand saturation like behavior. Additional immunostaining for lower TNC concentrations is provided in Fig. S6B (SI).

A key takeaway from these data is that dose and presentation mode matter equally to ligand identity. Although our work was not performed explicitly on ligand binding or clustering, for integrin-binding ligands like RGD, cell adhesion and downstream fate decisions are highly sensitive to ligand density, spacing, and clustering, because focal adhesion assembly requires productive integrin engagement rather than maximal occupancy. When adhesive ligands are presented at non-optimal densities/organization, cells can show impaired spreading and altered cytoskeletal organization, even when the ligand is "pro-adhesive" in principle. This general dependence on ligand density/organization is well established across engineered biomaterial surfaces and nanopatterned systems.[51,62]

In contrast, TNC functions as a context-dependent extracellular matrix cue whose biological activity is strongly influenced by its mode of presentation. Unlike generic adhesive ligands, TNC has been shown to modulate cell adhesion, migration, and differentiation in a spatially regulated manner, often exerting distinct effects when immobilized within the extracellular matrix *versus* presented in soluble form. Matrix-bound TNC can provide sustained, localized receptor engagement and cooperative signaling that is not achieved through soluble exposure alone, particularly in neural systems where ECM cues integrate with mechanotransductive pathways to regulate fate specification.[50]

The existence of a narrow concentration window in which immobilized TNC promotes neuronal and motor neuron differentiation further underscores the instructive, rather than purely permissive, role of this matrix protein. At higher surface densities, TNC may disrupt effective cell–matrix coupling through altered ligand conformation, receptor competition, or interference with integrin clustering, leading to reduced adhesion and impaired differentiation. Such dose-sensitive behavior is consistent with the role of TNC as a transient, remodeling-associated ECM component that is tightly regulated *in vivo* and associated with dynamic tissue states rather than stable homeostasis.[22,63]

Together, these findings support a model in which matrix-bound TNC acts as a potent, presentation-dependent instructive cue, capable of promoting neuronal differentiation when delivered within a defined concentration range. This behavior contrasts with that of generic integrin ligands and highlights the importance of ECM identity and immobilization strategy in engineering neural microenvironments.

3.5. 3D hydrogel experiments

To evaluate whether matrix-bound Tenascin-C retains its stimulatory effects in a three-dimensional environment, bulk MeHA hydrogels (1% w/v MeHA, 0.1% w/v LAP) were fabricated with immobilized TNC or RGD and assessed for structural stability, cytocompatibility, and neuronal differentiation, Fig. 5A shows the schematics for the experimental setup. Based on the 2D dose–response studies (Fig. 4) identifying ~100–200 nM immobilized TNC as optimal for βIII-tubulin and ISL1 expression, 100 nM TNC was selected for all 3D encapsulation experiments. RGD was incorporated at 100 μM as a benchmark integrin-binding ligand as validated in 2D experiments above.

Bulk MeHA constructs exhibited rapid swelling in phosphate-buffered saline at 37 °C, reaching equilibrium within approximately 6 hours as shown in Fig. 5B, consistent with stable hydrogel network formation. Enzymatic degradation studies further demonstrated material responsiveness, with hydrogels exposed to hyaluronidase (0.5 U per mL) undergoing progressive mass loss over seven days, while constructs maintained in PBS alone remained largely intact (Fig. 5C). These results confirmed that MeHA scaffolds possess high water content and physiologically relevant swelling behavior, reaching equilibrium swelling ratios of approximately 400% (hydrated mass/dry mass) within ~6 h in PBS at 37 °C (Fig. 5B). This degree of swelling is consistent with values reported for low-crosslink-density HA-based hydrogels[34,64] and reflects the high water content (~75–80%) characteristic of native spinal cord tissue,[65] confirming that the MeHA network recapitulates a key physicochemical property of the CNS extracellular environment and controlled enzymatic degradability. Rheological characterization of the 1% (w/v) bulk MeHA constructs revealed a storage modulus G' of approximately 0.3–0.7 kPa, corresponding to an estimated E_Y of ~0.8–1.3 kPa using $E_Y = 2G^*(1 + \nu)$ with $\nu = 0.5$ (Fig. 5D) (SI, Fig. S7). This places the 3D MeHA scaffold within the sub-kPa mechanical range characteristic of native CNS soft tissue and HA-based neural hydrogels reported in the literature,[34,64] providing a compliant, CNS-relevant environment for encapsulated cells. These experiments were performed to establish baseline swelling, degradation,

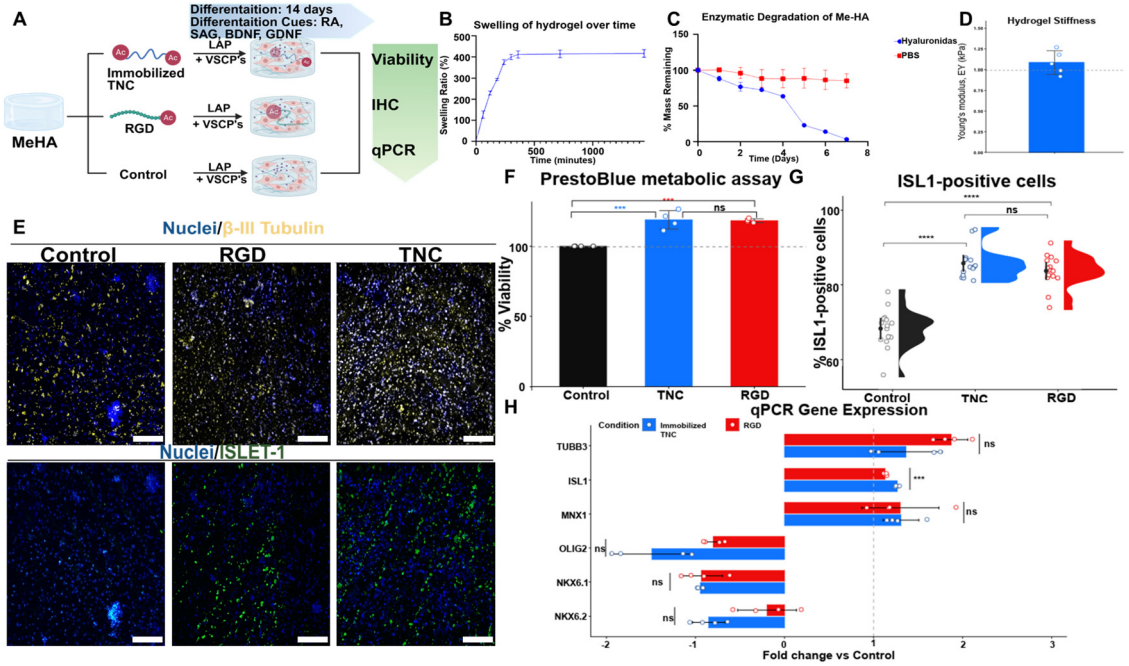

Fig. 5 Bulk MeHA hydrogels exhibit stability and support neuronal differentiation in 3D with immobilized Tenascin-C. (A) Schematic illustrating the differentiation timeline of human pluripotent stem cells into ventral spinal cord progenitors and motor neurons, and their encapsulation onto MeHA substrates functionalized with Tenascin-C (TNC) or RGD ligands. (B) Swelling kinetics of base bulk 1% MeHA hydrogels (0.1% LAP) incubated in PBS at 37 °C, showing rapid hydration and equilibrium swelling within ~6 h (n = 4). (C) Enzymatic degradation profile of bulk MeHA hydrogels incubated in hyaluronidase (0.5 U mL^{-1}) or PBS control at 37 °C, demonstrating enzyme-specific mass loss over time (n = 4). (D) Hydrogel stiffness characterization of bulk 1% MeHA constructs by rheological measurement, confirming sub-kPa mechanical properties within the range of native CNS tissue (n = 5). (E) Representative immunofluorescence images of cells encapsulated in bulk MeHA hydrogels showing neuronal and motor neuron marker expression (Nuclei, blue; βIII-tubulin, yellow; ISLET1, green). Scale bar: 50 μm. (F) PrestoBlue metabolic activity of cells cultured within bulk MeHA hydrogels functionalized with immobilized Tenascin-C (TNC) or RGD compared to unmodified controls (n = 4, S = 3). (G) Quantification of ISL1$^+$ cells in bulk hydrogels under control, TNC-, or RGD-functionalized conditions, presented as a raincloud plot combining half-violin density distributions (n = 3, S = 15 per group) with individual observations and mean ± 95% CI; brackets indicate Tukey HSD post-hoc comparisons following one-way ANOVA. (H) Quantitative PCR analysis of fold-change expression for six neuronal and motor neuron markers (TUBB3, ISL1, MNX1, OLIG2, NKX6.1, NKX6.2) in cells cultured in bulk hydrogels, shown as horizontal bar charts with individual data points Data are presented as mean ± SD (n = 4, S = 2) unless otherwise noted. Panels (F)–(H) were analyzed by Pairwise t-test. Statistical significance is indicated as * = $p < 0.05$, ** = $p < 0.01$, **** = $p < 0.0001$. Comparisons between RGD- and TNC-functionalized hydrogels were not statistically significant.

and mechanical behavior of the MeHA network prior to biochemical functionalization.

Following material characterization, the biological response of VSCP to functionalized MeHA hydrogels was evaluated. Both TNC and RGD functionalized constructs supported comparable or enhanced viability relative to control hydrogels, indicating that ligand incorporation and crosslinking did not compromise cytocompatibility. Immunohistochemical analysis at day 24 revealed robust neuronal differentiation within TNC and RGD functionalized hydrogels shown in Fig. 5E. Cell viability at day 24 within the 3D hydrogels remained high across all conditions, as assessed by Presto Blue metabolic assays in Fig. 5F. Gene expression analysis further supported these findings, with βIII-tubulin, MNX1 and ISL1(neuronal lineage/postmitotic motor neuron markers) expression significantly upregulated ($p < 0.005$) in TNC- and RGD-functionalized hydrogels relative to unmodified MeHA constructs; simultaneously Olig2, Nkx6-1, Nkx6-2 (Ventral progenitor markers) were downregulated in both TNC and RGD-functionalized hydrogels relative to control (Fig. 5H). βIII-tubulin expression marks commitment to the neuronal lineage, indicating that cells have exited the progenitor pool and initiated a neuronal differentiation program. ISL1 is a LIM homeodomain transcription factor that marks postmitotic motor neuron specification and is a definitive marker of motor neuron identity. Increased βIII-tubulin expression in both TNC- and RGD-functionalized 3D hydrogels therefore indicates that both functionalizations support neuronal lineage commitment, while the presence of ISL1-positive cells indicates progression toward motor neuron identity. Notably, immobilized TNC achieves these markers at substantially lower molar concentrations than RGD, supporting the interpretation that matrix-bound TNC is a more potent, presentation-dependent instructive cue rather than a generic adhesive ligand. Quantitative analysis further confirmed a significantly higher ($p < 0.005$) proportion of ISL1-positive cells in TNC- and RGD-modified hydrogels compared to controls (Fig. 5G).

The maintenance of neuronal and motor neuron differentiation in 3D MeHA supports the premise that matrix-tethered ECM cues can remain instructive when moved from 2D to a volumetric microenvironment, where soluble signals are more susceptible to dilution and transport limitations. Hydrogels are widely used for 3D culture specifically because they allow simultaneous control of network structure (swelling), degradability, and cue presentation, which together shape cell phenotype over time.[34,64,66] The swelling-to-equilibrium behavior and hyaluronidase-responsive mass loss are consistent with expected properties of HA-based hydrogels and support the use of MeHA as a remodelable matrix relevant to CNS-mimetic scaffold design.[34,67]

In this context, the observation that immobilized TNC induces neuronal markers at substantially lower concentrations than RGD is consistent with the view of TNC as a context-dependent, adhesion-modulatory ECM protein, whose signaling depends strongly on matrix presentation.[11,25,38,55] In future studies, this platform could be leveraged to assess whether matrix-tethered TNC promotes more advanced neuronal or motor neuron maturation, including the expression of late-stage markers and functional outcomes such as electrophysiological activity. Such studies would help clarify whether the efficiency of immobilized TNC translates into enhanced functional maturation relative to canonical adhesive ligands such as RGD. Together, these findings support MeHA as a stable 3D scaffold for presenting matrix-bound cues and motivate future designs that integrate tethered ECM signaling with controlled matrix remodeling for neural repair applications.[22,25,64,66]

Together, these results demonstrate that matrix-bound TNC retains its functional capacity to promote neuronal differentiation within bulk 3D MeHA hydrogels while maintaining material stability and cytocompatibility. This validates the translational relevance of the MeHA–TNC platform as a tunable scaffold for spinal cord injury repair, capable of integrating biochemical signaling with physiologically relevant mechanical and structural properties.

4. Conclusions

SCI induces dynamic remodeling of the ECM, including a transient upregulation of TNC during the subacute phase of tissue repair. By integrating *in vivo* transcriptional profiling with controlled *in vitro* biomaterial models, this study establishes a direct link between the temporal regulation of TNC following injury and its functional role in guiding neuronal differentiation when removed from the injury context.

Using stiffness-tunable MeHA hydrogels that decouple mechanical and biochemical cues, we demonstrated that matrix-bound TNC functions as an instructive ECM signal when presented within compliant, spinal cord-like environments. Immobilized TNC promoted neuronal and motor neuron differentiation more effectively than soluble TNC, underscoring the importance of ECM presentation mode in regulating cell fate decisions.

Importantly, TNC activity was found to be highly concentration dependent, with neuronal differentiation enhanced within a narrow window of surface-bound ligand density. While both 100 and 200 nM immobilized TNC supported robust βIII-tubulin expression, maximal ISL1 and MNX1 induction occurred at 100 nM, indicating that motor neuron specification is particularly sensitive to TNC dosage. In contrast, RGD-mediated responses scaled more broadly with concentration, consistent with generic integrin-driven adhesion rather than lineage-specific instruction. These findings highlight that ECM-derived signals do not operate in a linear or monotonic manner but instead require precise spatial and biochemical regulation to elicit desired cellular outcomes.

Extension of these findings into bulk 3D MeHA scaffolds confirmed that matrix-bound TNC retains its biofunctionality within physiologically relevant, degradable hydrogels, supporting neuronal differentiation while maintaining material stability and cytocompatibility. Together, this work establishes a design framework in which ECM-bound biochemical cues, presented within appropriately tuned mechanical environments, cooperatively define neural differentiation microenvironments.

Looking forward, these principles provide a foundation for the development of next-generation spinal cord injury scaffolds that integrate multiple ECM-derived signals in a spatially and mechanically controlled manner. Such combinatorial biomaterial strategies may enable more faithful recapitulation of the evolving post-injury niche and advance regenerative therapies for central nervous system repair.

Author contributions

R. P. designed and executed TNC purification and modification, all 2D and 3D *in vitro* experiments and subsequent analyses, spinal cord tissue sectioning, immunohistochemistry, gene expression analysis, 3D hydrogel rheology, and wrote and edited the manuscript. V. D. performed MeHA–PAA hydrogel fabrication and rheological characterization. J. O. performed the spinal cord contusion surgeries and animal care. E. E. performed atomic force microscopy measurements of spinal cord tissue stiffness. C. K. provided supervision and expertise for AFM studies. N. L. provided input towards study design, biomaterial scaffold development, and analyses, and provided funding support and critical input into all aspects of manuscript preparation and editing. All authors have given approval to the final version of the manuscript.

Conflicts of interest

There are no conflicts to declare.

Data availability

The datasets generated and/or analyzed during the current study are available from the corresponding author upon reasonable request.

Supplementary information (SI) is available. See DOI: https://doi.org/10.1039/d6tb00247a.

Acknowledgements

The authors would like to acknowledge partial funding from the National Science Foundation (NSF) Division of Chemical, Bioengineering, Environmental and Transport Systems (CBET) award numbers CBET-2042117 (University of Akron, PI N.D. Leipzig) and CBET-2042116 (Cleveland State University, PI C.R. Kothapalli) as well as partial funding from the Congressionally Directed Medical Research Programs (CDMRP) *via* the Spinal Cord Injury Research Program (SCIRP) award number SC220128.

References

1 J. Chen, H. Joon Lee, I. Jakovcevski, R. Shah, N. Bhagat, G. Loers, H.-Y. Liu, S. Meiners, G. Taschenberger, S. Kügler, A. Irintchev and M. Schachner, The Extracellular Matrix Glycoprotein Tenascin-C Is Beneficial for Spinal Cord Regeneration, *Mol. Ther.*, 2010, **18**(10), 1769–1777, DOI: 10.1038/mt.2010.133.

2 A. Alizadeh, S. M. Dyck and S. Karimi-Abdolrezaee, Traumatic Spinal Cord Injury: An Overview of Pathophysiology, Models and Acute Injury Mechanisms, *Front. Neurol.*, 2019, **10**, 282, DOI: 10.3389/fneur.2019.00282.

3 X. Hu, W. Xu, Y. Ren, Z. Wang, X. He, R. Huang, B. Ma, J. Zhao, R. Zhu and L. Cheng, Spinal Cord Injury: Molecular Mechanisms and Therapeutic Interventions, *Signal Transduct. Target. Ther.*, 2023, **8**(1), 245, DOI: 10.1038/s41392-023-01477-6.

4 A. Mohammed Butt, V. Rupareliya, A. Hariharan and H. Kumar, Building a Pathway to Recovery: Targeting ECM Remodeling in CNS Injuries, *Brain Res.*, 2023, **1819**, 148533, DOI: 10.1016/j.brainres.2023.148533.

5 Z. Xu, Y. Li, P. Li, Y. Sun, S. Lv, Y. Wang, X. He, J. Xu, Z. Xu, L. Li and Y. Li, Soft Substrates Promote Direct Chemical Reprogramming of Fibroblasts into Neurons, *Acta Biomater.*, 2022, **152**, 255–272, DOI: 10.1016/j.actbio.2022.08.049.

6 J. M. Stukel and R. K. Willits, Mechanotransduction of Neural Cells Through Cell–Substrate Interactions, *Tissue Eng., Part B*, 2016, **22**(3), 173–182, DOI: 10.1089/ten.teb.2015.0380.

7 Z. Lv, C. Dong, T. Zhang and S. Zhang, Hydrogels in Spinal Cord Injury Repair: A Review, *Front. Bioeng. Biotechnol.*, 2022, **10**, 931800, DOI: 10.3389/fbioe.2022.931800.

8 R. Pokharel and N. D. Leipzig, 3D Bioprinting for Spinal Cord Injury: Engineering Scaffolds for Functional Recovery, *ACS Biomater. Sci. Eng.*, 2026, **12**(2), 757–772, DOI: 10.1021/acsbiomaterials.5c01474.

9 P. L. Jones and F. S. Jones, Tenascin-C in Development and Disease: Gene Regulation and Cell Function, *Matrix Biol.*, 2000, **19**(7), 581–596, DOI: 10.1016/S0945-053X(00)00106-2.

10 F. S. Jones and P. L. Jones, The Tenascin Family of ECM Glycoproteins: Structure, Function, and Regulation during Embryonic Development and Tissue Remodeling, *Dev. Dyn.*, 2000, **218**(2), 235–259, DOI: 10.1002/(SICI)1097-0177(200006)218:2<235::AID-DVDY2>3.0.CO;2-G.

11 R. Chiquet-Ehrismann and R. P. Tucker, Tenascins and the Importance of Adhesion Modulation, *Cold Spring Harb. Perspect. Biol.*, 2011, **3**(5), a004960–a004960, DOI: 10.1101/cshperspect.a004960.

12 E. Dzyubenko, D. Manrique-Castano, M. Pillath-Eilers, P. Vasileiadou, J. Reinhard, A. Faissner and D. M. Hermann, Tenascin-C Restricts Reactive Astrogliosis in the Ischemic Brain, *Matrix Biol.*, 2022, **110**, 1–15, DOI: 10.1016/j.matbio.2022.04.003.

13 H. P. Erickson and H. C. Taylor, Hexabrachion Proteins in Embryonic Chicken Tissues and Human Tumors, *J. Cell Biol.*, 1987, **105**(3), 1387–1394, DOI: 10.1083/jcb.105.3.1387.

14 H. Zhang, L. Zhou, H. Wang, W. Gu, Z. Li, J. Sun, X. Wei and Y. Zheng, Tenascin-C-EGFR Activation Induces Functional Human Satellite Cell Proliferation and Promotes Wound-Healing of Skeletal Muscles via Oleanic Acid, *Dev. Biol.*, 2023, **504**, 86–97, DOI: 10.1016/j.ydbio.2023.09.010.

15 M. Tucić, V. Stamenković and P. Andjus, The Extracellular Matrix Glycoprotein Tenascin C and Adult Neurogenesis, *Front. Cell Dev. Biol.*, 2021, **9**, 674199, DOI: 10.3389/fcell.2021.674199.
16 K. S. Midwood and G. Orend, The Role of Tenascin-C in Tissue Injury and Tumorigenesis, *J. Cell Commun. Signal.*, 2009, **3**(3–4), 287–310, DOI: 10.1007/s12079-009-0075-1.
17 S. P. Giblin and K. S. Midwood, Tenascin-C: Form versus Function, *Cell Adhes. Migr.*, 2015, **9**(1–2), 48–82, DOI: 10.4161/19336918.2014.987587.
18 N. J. Gutowski, J. Newcombe and M. L. Cuzner, Tenascin-R and C in Multiple Sclerosis Lesions: Relevance to Extracellular Matrix Remodelling, *Neuropathol. Appl. Neurobiol.*, 1999, **25**(3), 207–214, DOI: 10.1046/j.1365-2990.1999.00176.x.
19 Y. Wang, G. Wang and H. Liu, Tenascin-C: A Key Regulator in Angiogenesis during Wound Healing, *Biomolecules*, 2022, **12**(11), 1689, DOI: 10.3390/biom12111689.
20 K. Omori, A. Takada, Y. Toyomasu, I. Tawara, C. Shintoku, K. Imanaka-Yoshida, H. Sakuma and Y. Nomoto, Expression of Tenascin-C Is Upregulated in the Early Stages of Radiation Pneumonitis/Fibrosis in a Novel Mouse Model, *Curr. Issues Mol. Biol.*, 2024, **46**(9), 9674–9685, DOI: 10.3390/cimb46090575.
21 C. Abi-Ghanem, D. Jonnalagadda, J. Chun, Y. Kihara and B. Ranscht, CAQK, a Peptide Associating with Extracellular Matrix Components Targets Sites of Demyelinating Injuries, *Front. Cell. Neurosci.*, 2022, **16**, 908401, DOI: 10.3389/fncel.2022.908401.
22 D. Bijelić, M. Adžić, M. Perić, G. Reiss, M. Milošević, P. R. Andjus and I. Jakovčevski, Tenascin-C Fibronectin D Domain Is Involved in the Fine-Tuning of Glial Response to CNS Injury in Vitro, *Front. Cell Dev. Biol.*, 2022, **10**, 952208, DOI: 10.3389/fcell.2022.952208.
23 D. Bijelić, M. Adžić, M. Perić, I. Jakovčevski, E. Förster, M. Schachner and P. R. Andjus, Different Functions of Recombinantly Expressed Domains of Tenascin-C in Glial Scar Formation, *Front. Immunol.*, 2021, **11**, 624612, DOI: 10.3389/fimmu.2020.624612.
24 Y.-L. Jin, S.-W. Bao, M.-X. Huang, Y.-J. Gao, H.-J. Lu and X.-B. Wu, The Role of Tenascin-C in Neuroinflammation and Neuroplasticity, *Int. J. Mol. Sci.*, 2025, **26**(20), 10174, DOI: 10.3390/ijms262010174.
25 K. Glotzbach and A. Faissner, Substrate-Bound and Soluble Domains of Tenascin-C Regulate Differentiation, Proliferation and Migration of Neural Stem and Progenitor Cells, *Front. Cell. Neurosci.*, 2024, **18**, 1357499, DOI: 10.3389/fncel.2024.1357499.
26 J. G. Cooper, D. Sicard, S. Sharma, S. Van Gulden, T. L. McGuire, M. P. Cajiao, D. J. Tschumperlin and J. A. Kessler, Spinal Cord Injury Results in Chronic Mechanical Stiffening, *J. Neurotrauma*, 2020, **37**(3), 494–506, DOI: 10.1089/neu.2019.6540.
27 T. Saxena, J. Gilbert, D. Stelzner and J. Hasenwinkel, Mechanical Characterization of the Injured Spinal Cord after Lateral Spinal Hemisection Injury in the Rat, *J. Neurotrauma*, 2012, **29**(9), 1747–1757, DOI: 10.1089/neu.2011.1818.
28 Y. Ma, H. Shi, Q. Wei, Q. Deng, J. Sun, Z. Liu, B. Lai, G. Li, Y. Ding, W. Niu, Y. Zeng and X. Zeng, Developing a Mechanically Matched Decellularized Spinal Cord Scaffold for the in Situ Matrix-Based Neural Repair of Spinal Cord Injury, *Biomaterials*, 2021, **279**, 121192, DOI: 10.1016/j.biomaterials.2021.121192.
29 S.-H. Kim, J. Turnbull and S. Guimond, Extracellular Matrix and Cell Signalling: The Dynamic Cooperation of Integrin, Proteoglycan and Growth Factor Receptor, *J. Endocrinol.*, 2011, **209**(2), 139–151, DOI: 10.1530/JOE-10-0377.
30 C.-W. Chiu, H. Cheng and S.-L. Hsieh, Contusion Spinal Cord Injury Rat Model, *Biol. Protoc.*, 2017, **7**(12), 2337, DOI: 10.21769/BioProtoc.2337.
31 J. Joshi, G. Mahajan and C. R. Kothapalli, Three-dimensional Collagenous Niche and Azacytidine Selectively Promote Time-dependent Cardiomyogenesis from Human Bone Marrow-derived MSC Spheroids, *Biotechnol. Bioeng.*, 2018, **115**(8), 2013–2026, DOI: 10.1002/bit.26714.
32 X. Shi and P. A. Janmey, Large Polyacrylamide Hydrogels for Large-Batch Cell Culture and Mechanobiological Studies, *Macromol. Biosci.*, 2023, **23**(9), 2300042, DOI: 10.1002/mabi.202300042.
33 H. J. Baumann, G. Mahajan, T. R. Ham, P. Betonio, C. R. Kothapalli, L. P. Shriver and N. D. Leipzig, Softening of the Chronic Hemi-Section Spinal Cord Injury Scar Parallels Dysregulation of Cellular and Extracellular Matrix Content, *J. Mech. Behav. Biomed. Mater.*, 2020, **110**, 103953, DOI: 10.1016/j.jmbbm.2020.103953.
34 J. A. Burdick, C. Chung, X. Jia, M. A. Randolph and R. Langer, Controlled Degradation and Mechanical Behavior of Photopolymerized Hyaluronic Acid Networks, *Biomacromolecules*, 2005, **6**(1), 386–391, DOI: 10.1021/bm049508a.
35 I. Aukhil, C. C. Slemp, V. A. Lightner, K. Nishimura, G. Briscoe and H. P. Erickson, Purification of Hexabrachion (Tenascin) from Cell Culture Conditioned Medium, and Separation from a Cell Adhesion Factor, *Matrix*, 1990, **10**(2), 98–111, DOI: 10.1016/S0934-8832(11)80176-9.
36 M. Wind and A. Tsakiridis, In Vitro Generation of Posterior Motor Neurons from Human Pluripotent Stem Cells, *Curr. Protoc.*, 2021, **1**(9), e244, DOI: 10.1002/cpz1.244.
37 K. J. Livak and T. D. Schmittgen, Analysis of Relative Gene Expression Data Using Real-Time Quantitative PCR and the $2-\Delta\Delta CT$ Method, *Methods*, 2001, **25**(4), 402–408, DOI: 10.1006/meth.2001.1262.
38 J. Chen, H. Joon Lee, I. Jakovcevski, R. Shah, N. Bhagat, G. Loers, H.-Y. Liu, S. Meiners, G. Taschenberger, S. Kügler, A. Irintchev and M. Schachner, The Extracellular Matrix Glycoprotein Tenascin-C Is Beneficial for Spinal Cord Regeneration, *Mol. Ther.*, 2010, **18**(10), 1769–1777, DOI: 10.1038/mt.2010.133.
39 A. Dobbertin, S. Czvitkovich, U. Theocharidis, J. Garwood, M. R. Andrews, F. Properzi, R. Lin, J. W. Fawcett and A. Faissner, Analysis of Combinatorial Variability Reveals

Selective Accumulation of the Fibronectin Type III Domains B and D of Tenascin-C in Injured Brain, *Exp. Neurol.*, 2010, **225**(1), 60–73, DOI: 10.1016/j.expneurol.2010.04.019.

40 E. J. Bradbury and E. R. Burnside, Moving beyond the Glial Scar for Spinal Cord Repair, *Nat. Commun.*, 2019, **10**(1), 3879, DOI: 10.1038/s41467-019-11707-7.

41 E. Moeendarbary, I. P. Weber, G. K. Sheridan, D. E. Koser, S. Soleman, B. Haenzi, E. J. Bradbury, J. Fawcett and K. Franze, The Soft Mechanical Signature of Glial Scars in the Central Nervous System, *Nat. Commun.*, 2017, **8**(1), 14787, DOI: 10.1038/ncomms14787.

42 A. Buxboim, J. Irianto, J. Swift, A. Athirasala, J.-W. Shin, F. Rehfeldt and D. E. Discher, Coordinated Increase of Nuclear Tension and Lamin-A with Matrix Stiffness Outcompetes Lamin-B Receptor That Favors Soft Tissue Phenotypes, *Mol. Biol. Cell*, 2017, **28**(23), 3333–3348, DOI: 10.1091/mbc.e17-06-0393.

43 R. J. Pelham and Y. Wang, Cell Locomotion and Focal Adhesions Are Regulated by Substrate Flexibility, *Proc. Natl. Acad. Sci. U. S. A.*, 1997, **94**(25), 13661–13665, DOI: 10.1073/pnas.94.25.13661.

44 J. R. Tse and A. J. Engler, Preparation of Hydrogel Substrates with Tunable Mechanical Properties, *Curr. Protoc. Cell Biol.*, 2010, **47**(1), 10.16.1–10.16.16, DOI: 10.1002/0471143030.cb1016s47.

45 P. Moshayedi, F. da, L. Costa, A. Christ, S. P. Lacour, J. Fawcett, J. Guck and K. Franze, Mechanosensitivity of Astrocytes on Optimized Polyacrylamide Gels Analyzed by Quantitative Morphometry, *J. Phys.: Condens. Matter*, 2010, **22**(19), 194114, DOI: 10.1088/0953-8984/22/19/194114.

46 K. Saha, A. J. Keung, E. F. Irwin, Y. Li, L. Little, D. V. Schaffer and K. E. Healy, Substrate Modulus Directs Neural Stem Cell Behavior, *Biophys. J.*, 2008, **95**(9), 4426–4438, DOI: 10.1529/biophysj.108.132217.

47 N. D. Leipzig and M. S. Shoichet, The Effect of Substrate Stiffness on Adult Neural Stem Cell Behavior, *Biomaterials*, 2009, **30**(36), 6867–6878, DOI: 10.1016/j.biomaterials.2009.09.002.

48 R. O. Hynes, The Extracellular Matrix: Not Just Pretty Fibrils, *Science*, 2009, **326**(5957), 1216–1219, DOI: 10.1126/science.1176009.

49 K. S. Midwood, M. Chiquet, R. P. Tucker and G. Orend, Tenascin-C at a Glance, *J. Cell Sci.*, 2016, **129**(23), 4321–4327, DOI: 10.1242/jcs.190546.

50 R. Chiquet-Ehrismann and R. P. Tucker, Tenascins and the Importance of Adhesion Modulation, *Cold Spring Harb. Perspect. Biol.*, 2011, **3**(5), a004960–a004960, DOI: 10.1101/cshperspect.a004960.

51 S. P. Massia and J. A. Hubbell, An RGD Spacing of 440 Nm Is Sufficient for Integrin Alpha V Beta 3-Mediated Fibroblast Spreading and 140 Nm for Focal Contact and Stress Fiber Formation, *J. Cell Biol.*, 1991, **114**(5), 1089–1100, DOI: 10.1083/jcb.114.5.1089.

52 C. Yu, J. B. K. Law, M. Suryana, H. Y. Low and M. P. Sheetz, Early Integrin Binding to Arg-Gly-Asp Peptide Activates Actin Polymerization and Contractile Movement That Stimulates Outward Translocation, *Proc. Natl. Acad. Sci. U. S. A.*, 2011, **108**(51), 20585–20590, DOI: 10.1073/pnas.1109485108.

53 J. Seong, A. Tajik, J. Sun, J.-L. Guan, M. J. Humphries, S. E. Craig, A. Shekaran, A. J. García, S. Lu, M. Z. Lin, N. Wang and Y. Wang, Distinct Biophysical Mechanisms of Focal Adhesion Kinase Mechanoactivation by Different Extracellular Matrix Proteins, *Proc. Natl. Acad. Sci. U. S. A.*, 2013, **110**(48), 19372–19377, DOI: 10.1073/pnas.1307405110.

54 R. P. Tucker and R. Chiquet-Ehrismann, Tenascin-C: Its Functions as an Integrin Ligand, *Int. J. Biochem. Cell Biol.*, 2015, **65**, 165–168, DOI: 10.1016/j.biocel.2015.06.003.

55 M. Chiquet, Tenascin-C: From Discovery to Structure-Function Relationships, *Front. Immunol.*, 2020, **11**, 611789, DOI: 10.3389/fimmu.2020.611789.

56 M. A. Ghert, W. Qi, H. P. Erickson, J. A. Block and S. P. Scully, Tenascin-C Splice Variant Adhesive/Anti-Adhesive Effects on Chondrosarcoma Cell Attachment to Fibronectin, *Cell Struct. Funct.*, 2001, **26**(3), 179–187, DOI: 10.1247/csf.26.179.

57 R. Chiquet-Ehrismann and M. Chiquet, Tenascins: Regulation and Putative Functions during Pathological Stress, *J. Pathol.*, 2003, **200**(4), 488–499, DOI: 10.1002/path.1415.

58 M. B. Wenk, K. S. Midwood and J. E. Schwarzbauer, Tenascin-C Suppresses Rho Activation, *J. Cell Biol.*, 2000, **150**(4), 913–920, DOI: 10.1083/jcb.150.4.913.

59 K. Imanaka-Yoshida and H. Aoki, Tenascin-C and Mechanotransduction in the Development and Diseases of Cardiovascular System, *Front. Physiol.*, 2014, **5**, 283, DOI: 10.3389/fphys.2014.00283.

60 T. Ishigaki, K. Imanaka-Yoshida, N. Shimojo, S. Matsushima, W. Taki and T. Yoshida, Tenascin-C Enhances Crosstalk Signaling of Integrin Avβ3/PDGFR-β Complex by SRC Recruitment Promoting PDGF-induced Proliferation and Migration in Smooth Muscle Cells, *J. Cell Physiol.*, 2011, **226**(10), 2617–2624, DOI: 10.1002/jcp.22614.

61 K. S. Midwood and J. E. Schwarzbauer, Tenascin-C Modulates Matrix Contraction via Focal Adhesion Kinase– and Rho-Mediated Signaling Pathways, *Mol. Biol. Cell*, 2002, **13**(10), 3601–3613, DOI: 10.1091/mbc.e02-05-0292.

62 U. Hersel, C. Dahmen and H. Kessler, RGD Modified Polymers: Biomaterials for Stimulated Cell Adhesion and Beyond, *Biomaterials*, 2003, **24**(24), 4385–4415, DOI: 10.1016/S0142-9612(03)00343-0.

63 M. Momčilović, V. Stamenković, M. Jovanović, P. R. Andjus, I. Jakovčevski, M. Schachner and Đ. Miljković, Tenascin-C Deficiency Protects Mice from Experimental Autoimmune Encephalomyelitis, *J. Neuroimmunol.*, 2017, **302**, 1–6, DOI: 10.1016/j.jneuroim.2016.12.001.

64 S. R. Caliari and J. A. Burdick, A Practical Guide to Hydrogels for Cell Culture, *Nat. Methods*, 2016, **13**(5), 405–414, DOI: 10.1038/nmeth.3839.

65 R. M. LoPachin, C. M. Castiglia and A. J. Saubermann, Elemental Composition and Water Content of Myelinated

Axons and Glial Cells in Rat Central Nervous System, *Brain Res.*, 1991, **549**(2), 253–259, DOI: 10.1016/0006-8993(91)90465-8.

66 I. Pereira, M. J. Lopez-Martinez, A. Villasante, C. Introna, D. Tornero, J. M. Canals and J. Samitier, Hyaluronic Acid-Based Bioink Improves the Differentiation and Network Formation of Neural Progenitor Cells, *Front. Bioeng. Biotechnol.*, 2023, **11**, 1110547, DOI: 10.3389/fbioe.2023.1110547.

67 C. B. Highley, G. D. Prestwich and J. A. Burdick, Recent Advances in Hyaluronic Acid Hydrogels for Biomedical Applications, *Curr. Opin. Biotechnol*, 2016, **40**, 35–40, DOI: 10.1016/j.copbio.2016.02.008.

